Check for updates

# Structural and electronic changes in the Ni$_{13}$@Ag$_{42}$ nanoparticle under surface oxidation: the role of silver coating†

R. H. Aguilera-del-Toro, (iD) *[a] F. Aguilera-Granja (iD) [b] and A. Vega[a]

Icosahedral Ni$_{13}$@Ag$_{42}$ is a stable nanoparticle formed by a magnetic nickel core surrounded by a silver coating that provides physical protection to the 3d metal cluster as well as antibacterial properties. In this work, we report density functional theoretical calculations to delve into a comprehensive analysis of how surface oxidation impacts the structural, electronic, magnetic, and reactivity properties of this interesting nanoparticle. To elucidate the role played by the silver coating, we compare the results with those found for the bare Ni$_{13}$ cluster also subjected to surface oxidation. When Ni$_{13}$ is covered by silver, we find a markedly robust behavior of the magnetic moment of the resulting nanoparticle, which remains nearly constant upon oxidation up to the rates explored, and the same holds for its overall reactivity. The obtained trends are rationalized in terms of the complex interplay between Ni–Ag and Ag–O interactions which impact the relative inter-atomic distances, charge transfer effects, spin polarization and magnetic couplings.

## 1 Introduction

Magnetic nanoparticles have emerged as a prominent subject in Materials Science, due to their crucial roles in a wide range of applications such as drug delivery,[1–4] tissue engineering,[5,6] biosensing,[7,8] magnetic resonance imaging,[4,9,10] ultrahigh density data storage,[11,12] magneto-electric memory devices[13] and surface deposition for diverse applications.[14–16] For applications operating in the superparamagnetic regime, nanoparticles based on 3d transition metals (TM) are considered highly suitable due to their low magnetic anisotropy energy, cost-effectiveness, and in some cases, biocompatibility. To optimize these magnetic nanoparticles for specific applications or to ensure the stability of their properties (*e.g.*, magnetic moment) in particular environments or processes, functionalization techniques are commonly employed. It is well-known that the magnetic properties of transition metals[17,18] are influenced by their corrosion. The impact of different environments, such as CO[19–23] and O$_2$,[24] on nickel and another transition metal clusters has been extensively studied, revealing a decrease in the magnetic moment.

The structural evolution of metallic clusters when exposed to various environments significantly affects their properties.[21–23,25–29]

*[a] Departamento de Física Teórica, Atómica y Óptica, Universidad de Valladolid, ES-47011 Valladolid, Spain. E-mail: rodrigohumberto.aguilera@uva.es*

*[b] Instituto de Física, Universidad Autónoma de San Luis Potosí, San Luis Potosí, Mexico*

For gold nanoclusters,[22] calculations underscore the significance of both surface coverage and the location of adsorbed oxygen in influencing the stability of co-adsorbed crotonaldehyde, the desired product in crotyl alcohol selox, while for paladium nanoclusters,[23] elevated CO coverages favored the formation of bridge-bound CO bonds, with some hollow-bound CO. The study predicted a coverage-dependent spectroscopic blue-shift in vibrational IR bands of adsorbed CO, coinciding with a 3.5% expansion of the palladium nanoparticle.

In a recent study by Vernieres *et al.*,[25] the influence of air exposure on the energetic and structural properties of silver clusters, composed of up to 3000 atoms and deposited on a layer of amorphous carbon, was investigated. Their findings indicated that air exposure led to a prevalence of icosahedral isomers among the observed ordered structures. One method for preventing the oxidation of Ni involves applying a silver Ag coating on the surface of Ni nanoparticles.[30–34] This approach not only offers physical protection but also induces alterations in the system properties. For instance, it can enhance electrical conductivity,[31,32] enable tunable piezoresistivity[33] or reduce toxic agents in water.[34]

In our previous work,[35] we employed density functional theory to examine the stability, chemical order, structural parameters, electronic structures, and magnetic properties of Ag$_x$Ni$_{55-x}$ icosahedral nanoalloys across the entire composition range. Our investigation revealed that Ni atoms tended to occupy internal positions within segregated structures, some of which exhibited exceptional stability in terms of both binding energy and excess energy. Notably, Ni$_{13}$@Ag$_{42}$ exhibited a

This journal is © the Owner Societies 2024

*Phys. Chem. Chem. Phys.*, 2024, **26**, 3117–3125 | **3117**

perfect core/shell configuration, with a substantial core composed of 13 Ni atoms, making it an ideal candidate for a nanomagnet. The silver coating provided physical protection for the 3d metal cluster, while also offering known antibacterial properties.[36–38]

Ni$_{13}$@Ag$_{42}$ displayed intriguing intrinsic magnetic properties. The Ni$_{13}$ core essentially retains the magnetic moment of the bare free cluster when covered by Ag, resulting in a nanoparticle with a localized magnetic moment in the core. The projected densities of states demonstrated that the highest occupied molecular orbital (HOMO) exhibited a Ni character, indicating that despite the weak Ag–Ni interaction and the protective role of Ag, Ni states could still play a substantial role in the reactivity of this nanomagnet. Furthermore, the minority spin character of the HOMO elucidated the increase or decrease in its magnetic moment by 1 $\mu_B$ upon ionization or electron capture, respectively. Thus, driven by the observations of Vernieres et al. and our previous findings, we embarked on investigating the extent to which the Ag coating provides protection for the Ni core against external agents capable of chemical reactions. This question remains open and warrants further exploration, which is the focus of the present work.

One of the most common and unavoidable reactions in the natural environment is oxidation. In this study, we examine how the structural and electronic properties, particularly magnetism, of the Ni$_{13}$@Ag$_{42}$ nanomagnet are altered when a certain number of oxygen atoms bond to the surface. As we will demonstrate, the intricate interplay between Ni–Ag and Ag–O interactions yields a robust nanomagnet up to approximately 20% oxygen coverage. We discuss the changes in relative inter-atomic distances and magnetic couplings, and compare the results with those obtained for the bare Ni$_{13}$ cluster under oxidation to elucidate the role played by the silver coating.

Our theoretical approach mirrors that of our previous work,[35] and in the subsequent section, we provide a brief overview of the essential aspects related to the presence of oxygen. The following sections delve into the results, examining the effects of oxidation on structural properties, as well as electronic and magnetic properties. Finally, we summarize the main conclusions.

## 2 Theoretical approach

In this work we studied the surface oxidation process and how it affects the structural, electronic and magnetic properties of the metallic nanoalloy Ni$_{13}$@Ag$_{42}$ using the SIESTA code,[39] an efficient density functional theory implementation that solves the spin-polarized Kohn–Sham equations within the pseudopotential approach to treat the core interactions.

For the exchange and correlation (xc) potential we used the Perdew–Burke–Ernzerhof functional.[40] It is known that the standard GGA does not provide the exact (or quantitatively accurate) results concerning the magnetic (and other) properties of certain transition metal systems. DFT itself only provides a qualitative description of systems that are inherently multiconfigurational.

The magnetic moments predicted using the PBE functional for Ni clusters underestimate the experimental values. The same degree of inaccuracy of the PBE, however, is not extrapolatable to other Ni nanostructures like surfaces, or to the bulk for which the PBE functional gives the experimental magnetic moment. A better description of the intra-atomic Coulomb repulsion with a partial correction of the self-interaction error brings the standard DFT results closer to those predicted by quantum-chemical treatment through configuration-interaction approaches, which are unpracticable for these sizes. In this regard, a GGA+$U$ approach, or the employment of hybrid functionals should be, in principle, a good alternative to improve the description. In a recent work by A–G Boudjahem et al.,[21] devoted to the adsorption of CO on small Ni clusters, the hybrid BLYP functional (which incorporates a portion of exact exchange from Hartree–Fock theory) was employed. With this functional, the calculated properties of Ni$_2$ and CO compare well with the experimental data. But even with this functional, the predicted total magnetic moments for bare Ni clusters of 11 and 12 atoms (the largest size explored in their study) also underestimate the experimental values. By selecting an appropriate $U$ parameter in the GGA+$U$ approach one could fit the experimental magnetic moment for clusters, but overestimate the magnetic moment of the Ni bulk if the $U$ parameter is kept fixed. Since the main goal of our work is to understand the qualitative changes caused by the oxidation, we decided to use the PBE functional for the exchange–correlation treatment. We employed norm-conserving scalar relativistic pseudopotentials[41] in their fully nonlocal form,[42] generated from the atomic valence configuration 3d$^8$4s$^2$ for Ni (with core radii of 2.00, 2.44 and 2.50 a.u. for s, p and d orbitals, respectively), 4d$^{10}$5s$^1$ for Ag (with core radii of 2.17, 2.82 and 2.40 a.u. for s, p and d orbitals, respectively), and 2s$^2$2p$^4$ for O (with core radii of 1.14 for s, p and d orbitals). Non-linear partial core corrections,[43] which are known to be important for transition metal pseudopotentials, are included at the core radius of 0.7 Å. Valence states were described using double-$\zeta$ basis sets for Ni, Ag and O, with maximum cutoff radii of 4.931 Å (2p) and 7.998 Å (3d,4s). A 4p polarization orbital was also considered, with cutoff radii of 7.998 and 6.599 Å for nickel and silver respectively. The energy cutoff used to define the real-space grid for numerical calculations involving the electron density was 250 Ry. The Fermi distribution function that enters in the calculation of the density matrix was smoothed with an electronic temperature of 15 meV. We used an energy criterion of 10$^{-4}$ eV for converging the electronic density. In the calculations, the individual clusters were placed in a cubic supercell of 25 × 25 × 25 Å$^3$, a size large enough to neglect the interaction between the cluster and its replicas in neighboring cells. It was considered only the $\Gamma$ point ($k = 0$) when integrating over the Brillouin zone, as usual for finite systems. The equilibrium geometries resulted from an unconstrained conjugate-gradient structural relaxation using the DFT until the forces on each atom was smaller than 0.001 eV Å$^{-1}$. We tested in all cases different spin isomers to be sure of the ground state.

The local electronic charge and magnetic moments distribution within the nanomagnet were determined from the

**3118** | Phys. Chem. Chem. Phys., 2024, **26**, 3117–3125

This journal is © the Owner Societies 2024

Mulliken population. In those cases where the total energy difference between spin isomers was lower than 40 meV, we performed additional calculations with the same xc functional using the code VASP[44,45] that solves the Khon–Sham equations using a plane-waves basis set instead of numerical pseudoatomic orbitals, and the core interactions were treated be means of the Projector-Augmented-Wave (PAW) approach instead of pseudopotentials. The technical settings for the VASP calculations were as follows. We used the same cubic supercell as that used in SIESTA ($25 \times 25 \times 25$ Å$^3$) which we checked to be enough also with the plane waves basis set. An energy cutoff of 650 eV for the basis set was checked to provide converged results for the relevant magnitudes. As in SIESTA, the size chosen for the supercell allows us to use only the gamma point for the integrations in the Brillouin zone. Finally, an energy convergence criterion of $10^{-6}$ for the electronic density was considered. The structures were relaxed using conjugate gradients until the force on each atom was smaller than 0.001 eV Å$^{-1}$.

In order to study the stability of the magnetic nanoparticle as it oxidizes, we calculated the binding energy per atom, $E_b$ as well as the oxygen adsorption energy per oxygen atom, $E_{ads}$. To determine the relative stability of a given oxidation rate with respect to the neighboring rates, we calculated the second energy difference, $\Delta_2 E(x,y)$. These quantities are defined as follows:

$$E_b = [42E(\mathrm{Ag}) + 13E(\mathrm{Ni}) + mE(\mathrm{O}) - E(\mathrm{Ag}_{42}\mathrm{Ni}_{13}\mathrm{O}_m)]/(55 + m) \quad (1)$$

$$E_{ads} = \frac{E(\mathrm{Ag}_{42}\mathrm{Ni}_{13}) + mE(\mathrm{O}) - E(\mathrm{Ag}_{42}\mathrm{Ni}_{13}\mathrm{O}_m)}{m} \quad (2)$$

$$\Delta_2 E(m) = E(m+1) + E(m-1) - 2 \times E(m) \quad (3)$$

For the discussion of the reactivity, we calculated two conceptual DFT based quantities,[46–48] the electronegativity and the chemical hardness, respectively defined as:

$$\chi = -\mu = -\left(\frac{\partial E}{\partial N}\right)_\nu = \frac{1}{2}(\mathrm{IP} + \mathrm{EA}) \quad (4)$$

$$\eta = \frac{1}{2}E_{gap} = -\left(\frac{\partial^2 E}{\partial N^2}\right)_\nu = \frac{1}{2}(\mathrm{IP} - \mathrm{EA}) \quad (5)$$

where for a system of $N$ electrons, $\mathrm{IP} = E(N-1) - E(N)$ and $\mathrm{EA} = E(N) - E(N+1)$ are the vertical ionization potential and electronic affinity (calculated at the optimal geometry of the neutral system). These quantities are of fundamental importance in reactivity studies, as the electronic processes that occur in typical reactions are simply too fast as compared to vibrational frequencies.

## 3 Results

In our previous work,[35] we provided evidence for the favorable formation of Ni$_{13}$@Ag$_{42}$ compared to an ideal mixture of Ag$_{55}$ and Ni$_{55}$ clusters. We observed a distinct segregation between the atomic species within Ni$_{13}$@Ag$_{42}$. Notably, Ni$_{13}$@Ag$_{42}$ exhibited a significant decrease in excess energy and a pronounced increase in the second energy difference, indicating its remarkable relative stability compared to neighboring compositions. Furthermore, an analysis of the distribution of local magnetic moments confirmed that the magnetic moment is predominantly localized in the Ni core. In the following sections, we delve into a comprehensive analysis of how oxidation impacts the structural, electronic, and magnetic properties of the Ni$_{13}$ cluster, while also exploring the role played by the silver coating.

### 3.1 Oxidation process, structural and energetic properties

The surface oxidation process involved the sequential addition of individual oxygen atoms to the surface sites of Ni$_{13}$ (up to 10 atoms) and Ni$_{13}$@Ag$_{42}$ (up to 20 atoms). Molecular adsorption was found to be much less stable, as calculations showed that the oxygen molecule readily dissociates during the optimization process, indicating a low or absence of an energy barrier and suggesting that only dissociative chemisorption is relevant in this system at least in the first stages of oxidation.

To determine the ground state configurations of the oxidized nanomagnet, various initial locations were tested for each additional adsorbed oxygen atom among non-equivalent hollow, bridge, and top positions on the surface. Hollow sites were found to be the most stable adsorption sites. For the first oxygen atom, all possible sites were calculated, resulting in six non-equivalent sites: two tops, two bridges, and two hollows. Hollow positions were found to be more stable than bridge and top positions. Once the most stable adsorption site for a single oxygen atom was identified, it was kept fixed, and the optimal adsorption site for the next oxygen atom was explored. This process was repeated, adding oxygen atoms one at a time.

While this approach limits the number of sampled configurations, additional optimizations were performed for each oxygen concentration from Ni$_{13}$@Ag$_{42}$O$_2$ to Ni$_{13}$@Ag$_{42}$O$_6$. At least twenty configurations were randomly tested for each oxygen concentration, with oxygen absorbed at different positions on the surface. None of these arrangements had a lower energy than the putative ground state obtained using the method described earlier. Configurations with oxygen atoms inside the structure (subsurface) were also tested, but their energies were higher than when oxygen was absorbed at the surface. Moreover, it was observed that oxygen atoms tend to be absorbed in pairs near the silver atoms at the corners of the icosahedron, indicating an oxidation pattern that emerges early in the process.

Fig. 1 presents the putative ground state atomic configurations of Ni$_{13}$@Ag$_{42}$ during the oxidation process. Oxygen atoms preferentially occupy hollow sites near the corners of the icosahedron. The first oxygen atom is placed in a hollow site involving one of the 12 vertices, and subsequent oxygen atoms bind in another hollow site of the same vertex but non-adjacent to the previous ones. This pattern continues for the next couple of oxygen atoms throughout the oxidation process. To investigate the role of the silver coating and its effectiveness in
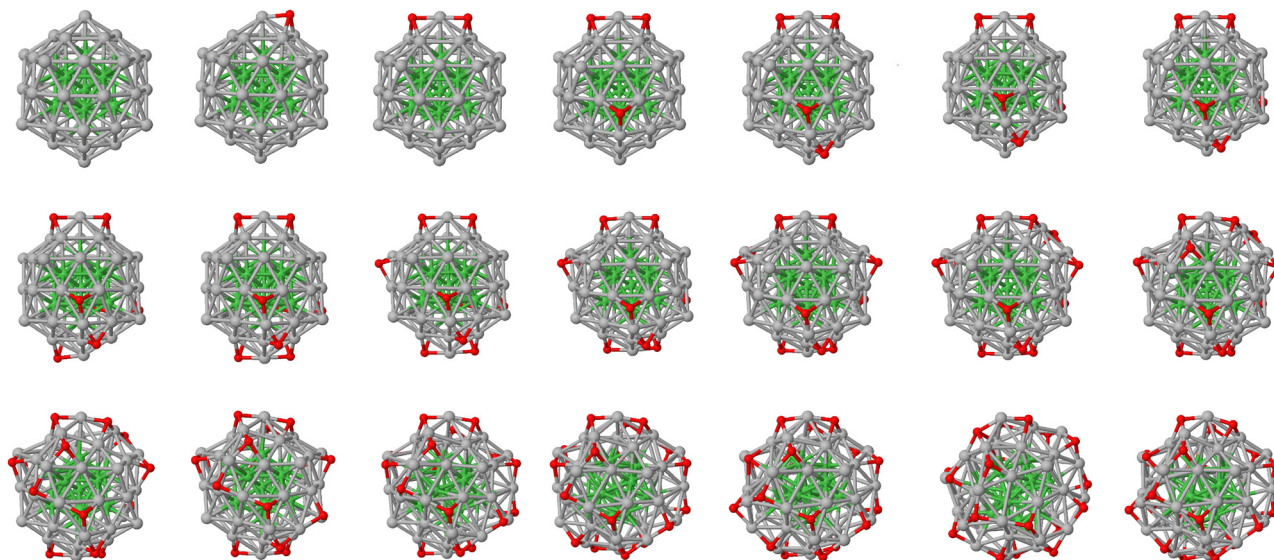
This journal is © the Owner Societies 2024

*Phys. Chem. Chem. Phys.*, 2024, **26**, 3117–3125 | **3119**

**Fig. 1** Putative ground state atomic configurations of Ni$_{13}$@Ag$_{42}$O$_m$ with $m$ = 1 to 20.

protecting the nickel core against oxidation, the same process was studied for the bare Ni$_{13}$ icosahedron cluster. The putative ground state atomic configurations are shown in Fig. 2. It is worth noting that in the 13-atom icosahedron, all vertices are connected to each other through hollow sites, unlike the 55-atom icosahedron. In the oxidation process of Ni$_{13}$, stable Ni$_3$O$_3$ ring motifs, known to be extremely stable arrangements,[24,49] can be identified.

To quantify the effect of oxidation on the structure of Ni$_{13}$ with and without the Ag coating, average interatomic distances and the total number of atomic bonds were plotted in Fig. 3 for both cases. The trends reveal the extent to which the silver coating physically protects the Ni core and preserves the structural identity of Ni$_{13}$ against oxidation. In the absence of oxygen, the average Ni–Ni distance is smaller in the bare Ni$_{13}$ cluster than in Ni$_{13}$@Ag$_{42}$, as expected due to the Ni–vacuum interface in the former. Upon oxidation, the average Ni–Ni distance rapidly increases in the bare Ni$_{13}$ cluster, while it remains almost constant (or slightly decreases) when surrounded by the 42 Ag atoms forming the Ni$_{13}$@Ag$_{42}$ nanoparticle. The average Ag–Ag and Ag–Ni interatomic distances increase as more Ag–O bonds are created. The number of Ni–Ni atomic bonds remains constant in both the Ni$_{13}$ cluster and the Ni$_{13}$@Ag$_{42}$ nanoalloy until sixteen oxygen atoms are absorbed on the Ag surface. A structural transition is observed in the nanoalloy when twelve oxygen atoms have been deposited on its surface, and this is reflected in the magnetic moment, as discussed later.

To evaluate the stability of the Ni$_{13}$@Ag$_{42}$ nanoparticle as a function of the oxidation rate, the relevant energetic quantities were calculated and plotted in Fig. 4. The increasing trend observed in the binding energy per atom suggests that the nanoparticle gains stability as it oxidizes within the explored regime. However, saturation of the binding energy has not yet been reached. Previous studies on transition metal oxide
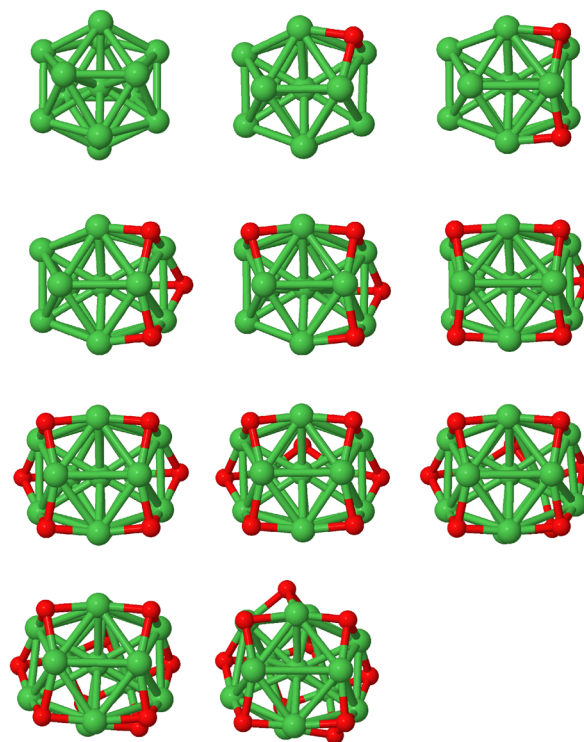


**Fig. 2** Putative ground state atomic configurations of Ni$_{13}$O$_m$ with $m$ = 1 to 10.

clusters have indicated that saturation occurs when almost all available surface sites are occupied, and subsequent oxidation takes the form of molecular O$_2$ adsorption.[18,50,51] In the present case, full surface oxidation has not been achieved (as shown in Fig. 1). Nevertheless, a slight negative curvature is noticeable in the binding energy, except at the beginning of the oxidation process and around Ag$_{42}$Ni$_{13}$O$_{16}$. This negative curvature

**3120** | *Phys. Chem. Chem. Phys.*, 2024, **26**, 3117–3125

This journal is © the Owner Societies 2024
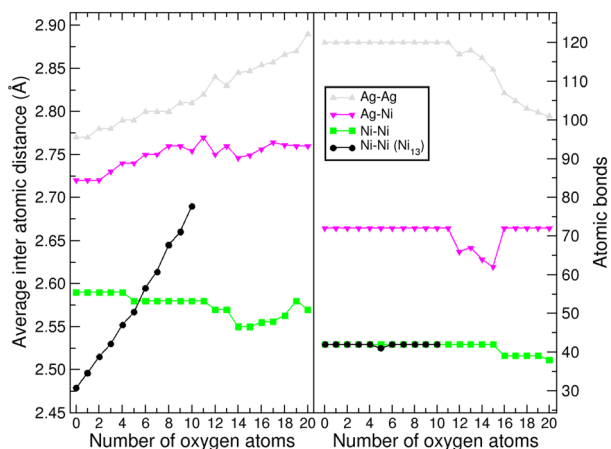
Fig. 3 Average inter-atomic distances (left panel) and number of atomic bonds (right panel) for $Ni_{13}@Ag_{42}O_m$ as functions of the oxygen content. In black, the Ni–Ni values for $Ni_{13}O_m$. We consider that two neighboring atoms form a bond when their inter-atomic distance is smaller than the average distance of those atoms in the non-oxidized system plus 10%.
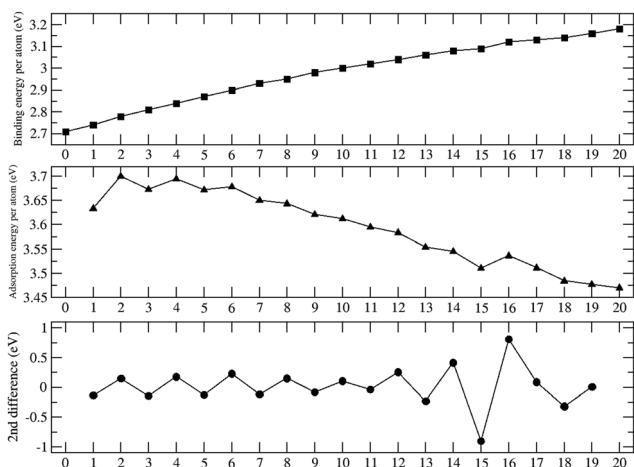


Fig. 4 Binding energy per atom (upper panel), oxygen adsorption energy (central panel), and second energy difference (lower panel) of $Ni_{13}@Ag_{42}O_m$ as a function of the oxidation rate.

corresponds to the overall decreasing behavior of the oxygen adsorption energy per oxygen atom, which also displays an oscillation at $m = 16$. These observations are attributed to the strong Ag–O bonding and suggest the eventual saturation of the binding energy at higher oxidation rates. The strong Ag–O bonding is consistent with the preservation of the structural identity of the $Ni_{13}$ core to a large extent. It is noteworthy that the anomalies in the energetic indicators found at $m = 16$ are also reflected in the structural parameters shown in Fig. 3.

The second energy difference indicates the relative stability with respect to neighboring oxidation rates (with one more or one less oxygen atom). An even–odd behavior is observed, with the system being more stable when it contains an even number of oxygen atoms on its surface. This trend aligns with the growth pattern observed, where pairs of oxygen atoms occupy

hollow sites around a given Ag vertex atom, ensuring an even distribution across the surface.

### 3.2 Electronic properties, magnetism and reactivity

In our previous work,[35] we discovered that the magnetic moment of $Ni_{13}@Ag_{42}$ primarily resides in the Ni core. Additionally, the magnetic moment of $Ni_{13}@Ag_{42}$ is equivalent to that of bare $Ni_{13}$, which is 8 $\mu_B$. However, while the magnetic moment of the central atom in the bare $Ni_{13}$ cluster points in the opposite direction to the moment of the shell atoms, no antiparallel couplings are observed in the Ni core of $Ni_{13}@Ag_{42}$, contributing 7.6 $\mu_B$ to the total moment. This indicates that the silver coating slightly reduces the spin polarization of the Ni core due to charge transfer effects, as discussed in the following paragraph. When both systems undergo oxidation, distinct behaviors are observed. In the case of $Ni_{13}$, the total magnetic moment significantly increases until it absorbs seven oxygen atoms ($m = 7$), reaching 14 $\mu_B$, but then abruptly decreases with further oxidation. Hence, oxidation strongly impacts the magnetic moment of the bare Ni cluster. In contrast, when $Ni_{13}$ is covered by silver, the resulting $Ni_{13}@Ag_{42}$ nanoparticle exhibits a more robust behavior of the moment. The total moment remains constant upon oxidation (8 $\mu_B$), except for a slight reduction to 6 $\mu_B$ from $m = 12$ to $m = 14$ and a slight increase to 10 $\mu_B$ for $m = 20$. Despite the decrease in the magnetic moment, the energy difference between the magnetic states of 6 and 8 $\mu_B$ is 30, 40, and 70 meV for $m = 12$, 13 and 14, respectively. For these systems, additional calculations were performed using the VASP code. In the cases with $m = 13$ and 14, the differences remain consistent with the SIESTA calculations. However, in the VASP calculation for $m = 12$, the magnetic moment of 6 $\mu_B$ is more stable than that of 8 $\mu_B$ by 3 meV, indicating that both spin states can be considered degenerate in this case. To understand this contrasting magnetic behavior under oxidation, we need to consider various aspects related to the direct binding of oxygen to Ni in the bare $Ni_{13}$ cluster compared to binding to Ag in $Ni_{13}@Ag_{42}$, which affects both the structural properties of the Ni core and the electronic interactions. As previously discussed, the bare $Ni_{13}$ cluster expands significantly with increasing oxidation rate, accompanied by an increasing delocalization of d electrons in $Ni_{13}$. This delocalization enhances spin polarization, leading to an increase in the Ni contribution to the total moment upon oxidation. However, this effect is not observed in $Ni_{13}@Ag_{42}$, where the electron delocalization is limited due to the presence of the silver coating. The local charge distribution obtained through the Mulliken populations reveals that $Ni_{13}$ is electron deficient, and this electron deficiency increases monotonically with oxidation. The charge transfer from Ni to O further promotes an increase in the magnetic moment during oxidation due to the more than half-filled d-band in Ni. In contrast, the Ni core of $Ni_{13}@Ag_{42}$ captures electrons from Ag, but this electron excess remains nearly constant (approximately 0.4 electrons per Ni atom) with increasing oxidation rate.

The distribution of local magnetic moments obtained from the Mulliken populations and presented in Fig. 5 reveals an
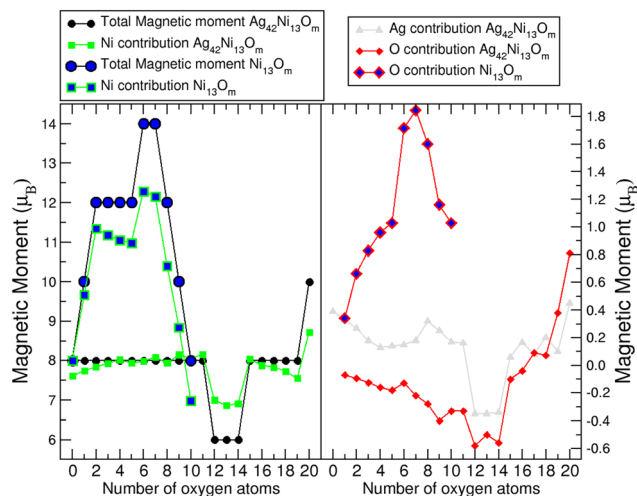
This journal is © the Owner Societies 2024

Phys. Chem. Chem. Phys., 2024, **26**, 3117–3125 | **3121**

**Fig. 5** Contribution of the different atomic species to the total magnetic moment of the magnetic nanoparticles.

increase in the moment of the bare Ni cluster up to $Ni_{13}O_7$, but no further increase with additional oxidation. As both the structural expansion and the charge transfer exhibit a monotonic trend, we need to analyze the local properties to explain the gradual decrease in the magnetic moment for $m \geq 7$. Our findings indicate that, for all investigated oxidation rates, the magnetic coupling is ferromagnetic-like. However, for $m \geq 7$, there is a noticeable reduction in spin polarization for certain Ni atoms. The local densities of electronic states (not shown here) show a transition from half metallic (with a spin-down character of the HOMO) to metallic behavior as a function of $m$, with a transition occurring around $m = 6$–7. Consequently, during the initial stages of oxidation ($m \leq 7$), the Ni to O charge transfer is predominantly contributed by spin-down electrons, resulting in an increase in the moment (even the spin-up band fills up slightly). Conversely, for $m \geq 7$, there is also transfer of spin-up electrons (more spin-up and fewer spin-down as m increases), which tends to reduce the magnetic moment.

On the other hand, the contribution of oxygen to the total moment varies depending on the atomic species it binds to. We observe that the spin polarization of oxygen atoms is significantly higher in $Ni_{13}O_m$ compared to $Ni_{13}@Ag_{42}O_m$. In the mean field picture, this can be attributed to the larger local magnetic field experienced by oxygen electrons when they attach to Ni (a magnetic 3d element) compared to when they attach to Ag, resulting in greater spin splitting in the former. Additionally, the spin polarization of the O atoms aligns with that of Ni in the bare $Ni_{13}$ (ferromagnetic-like coupling), causing the local moments to point in the same direction and contribute to the total moment. A substantial percentage of the magnetic moment is derived from the oxygen atoms, reaching over 13% in certain oxidation rates. Conversely, in $Ni_{13}@Ag_{42}$ (antiferromagnetic-like coupling), the situation is reversed until the adsorption of sixteen oxygen atoms, after which the oxygen exhibits ferromagnetic-like coupling with Ni.

The behavior of the magnetic moment in $Ni_{13}@Ag_{42}$ as a function of oxidation rate is also influenced by the structural anomalies discussed in the previous subsection. Between $Ni_{13}@$ $Ag_{42}O_{12}$ and $Ni_{13}@Ag_{42}O_{15}$, the magnetic moment slightly decreases from 8 to 6 $\mu_B$, correlating with a decrease in the average Ni–Ni interatomic distance and the number of Ag–Ni atomic bonds. These observations indicate that the Ni core becomes more compact and weakens its interaction with silver. At higher oxidation rates than $Ni_{13}@Ag_{42}O_{11}$, the average interatomic Ag–Ag distance increases, and the number of Ag–Ag atomic bonds decreases, indicating a weakening of the metallic silver character and the evolution of the surface from an oxidized metal to a metal oxide. In terms of corrosion, the protective coating forms a sacrificial layer upon oxidation to protect the core.

Lastly, the direct contribution of silver atoms to the magnetic moment of $Ni_{13}@Ag_{42}$ upon oxidation is analyzed. The local magnetic moment of silver atoms decreases as the system oxidizes. Although the spin splitting in Ag is negligible compared to that of nickel and oxygen, it is antiparallel to the $Ni_{13}@Ag_{42}$ nanoparticle, resulting in a constant total magnetic moment.

Let us now discuss the reactivity. The indicators of global reactivity are plotted in Fig. 6. Electronegativity ($\chi$) quantifies the nanoparticle's ability to attract and retain electrons, and the results demonstrate that electronegativity is lower in the $Ni_{13}@Ag_{42}$ nanoparticle than in the bare $Ni_{13}$ cluster, and increases with higher oxygen content. This aligns with the significantly higher electronegativity of O compared to Ni and Ag, making the surface more electropositive and consequently more reactive towards electrophilic agents such as additional oxygen. Therefore, further oxidation is expected to be faster and more exothermic, while reactivity towards nucleophilic agents will be reduced. However, a negative curvature indicates a tendency towards oxygen saturation and a progressive decrease in the aforementioned trend. Chemical hardness ($\eta$), defined as
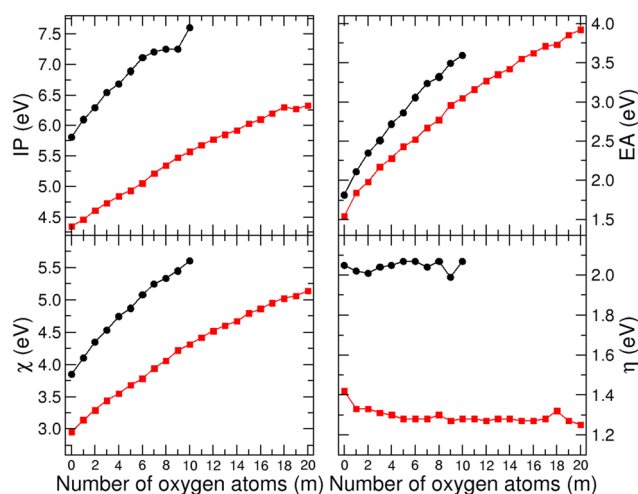


**Fig. 6** Indicators of global reactivity. Vertical ionization potential (IP), electronic affinity (EA), electronegativity ($\chi$) and chemical hardness ($\eta$). The black line corresponds to $Ni_{13}O_m$, while the red line represents $Ni_{13}@Ag_{42}O_m$.

**3122** | *Phys. Chem. Chem. Phys.*, 2024, **26**, 3117–3125

This journal is © the Owner Societies 2024

half the fundamental gap, quantifies the system's sensitivity to changes in the number of electrons. Higher hardness implies a reluctance to accept or donate electrons, correlating with lower polarizability. The results in Fig. 6 show that the chemical hardness is larger in the bare $Ni_{13}$ cluster than in the $Ni_{13}@Ag_{42}$ nanoparticle in which it remains nearly constant or slightly decreases with increasing oxidation rate. Both the ionization potential (IP) and electron affinity (EA) increase with oxygen content, but their difference remains relatively unchanged. This finding indicates that the overall reactivity of this nanomagnet is stable against oxidation, at least within the explored oxidation rate range.

## 4 Conclusions

In this study, we investigated the structural and electronic properties of the highly stable icosahedral $Ni_{13}@Ag_{42}$ nanoparticle using density functional theory. This nanoparticle consists of a nickel core and an outer silver shell. We examined how the interaction of oxygen atoms, up to a maximum of 20, on the surface of the nanoparticle affects its properties. To understand the role played by the silver coating, we compared our findings with the behavior of the bare $Ni_{13}$ cluster under surface oxidation.

Within the explored oxidation range, only dissociative chemisorption is relevant, as the oxygen molecule readily dissociates during the relaxation process. The absorbed oxygen atoms tend to form pairs near the silver atoms located at the corners of the $Ni_{13}@Ag_{42}$ nanoparticle, indicating a specific oxidation pattern.

Regarding the structural changes, our analysis of the relative inter-atomic distances revealed that the bare $Ni_{13}$ cluster is more compact than the $Ni_{13}$ core of the nanoparticle in the absence of oxygen. However, upon oxidation, the bare $Ni_{13}$ cluster expands, while the $Ni_{13}$ core of the nanoparticle remains almost constant and slightly compacts when more than 12 oxygen atoms attach. This difference can be attributed to the physical protection provided by the Ag coating.

From an energetic perspective, we observed that the $Ni_{13}@Ag_{42}$ nanoparticle becomes more stable as it undergoes oxidation. However, we have not yet reached saturation in the binding energy within the explored oxidation range. The relative stability of the nanoparticle compared to neighboring oxidation states follows an even–odd behavior, where the presence of an even number of oxygen atoms on the surface enhances the stability. This trend aligns with the observed growth pattern, where pairs of oxygen atoms occupy hollow sites around a given Ag vertex atom, ensuring an even distribution across the surface.

Regarding the magnetic properties, although the magnetic moment of $Ni_{13}@Ag_{42}$ (8 $\mu_B$) is equal to that of the bare $Ni_{13}$ cluster, the behaviors upon oxidation differ significantly. When $Ni_{13}$ is covered by silver, the resulting nanoparticle exhibits a remarkably robust magnetic moment that remains nearly constant throughout the oxidation process. In contrast, in the bare $Ni_{13}$ cluster, the total magnetic moment increases noticeably

until it absorbs seven oxygen atoms, reaching 14 $\mu_B$, and then abruptly decreases with further oxidation. This behavior can be explained in terms of relative charge transfer effects. The contribution of oxygen to the total moment varies depending on the atomic species it binds to. We observed that the spin polarization of oxygen atoms is significantly higher in $Ni_{13}O_m$ than in $Ni_{13}@Ag_{42}O_m$. Additionally, the spin polarization of the oxygen atoms aligns with that of Ni in the bare $Ni_{13}$ cluster, thus contributing to the total moment. In $Ni_{13}@Ag_{42}$, the situation is reversed until sixteen oxygen atoms are absorbed.

From a reactivity perspective, we have observed that the electronegativity of the $Ni_{13}@Ag_{42}$ nanoparticle increases with a higher oxygen content. This results in a more electropositive surface, making the nanoparticle more reactive towards electrophilic agents, such as additional oxygen. However, the reactivity towards nucleophilic agents is expected to decrease. Despite these changes, the chemical hardness of the nanoparticle remains relatively constant, indicating that the overall reactivity of this nanomagnet remains stable against oxidation within the explored range.

## Conflicts of interest

There are no conflicts to declare.

## Acknowledgements

## References

1 J. Dobson, Magnetic nanoparticles for drug delivery, *Drug Dev. Res.*, 2006, **67**(1), 55–60.

2 M. Arruebo, R. Fernández-Pacheco, M. R. Ibarra and J. Santamaría, Magnetic nanoparticles for drug delivery, *Nano Today*, 2007, **2**(3), 22–32.

3 S. C. McBain, H. H. Yiu and J. Dobson, Magnetic nanoparticles for gene and drug delivery, *Int. J. Nanomed.*, 2008, **3**(2), 169–180. PMID: 18686777.

4 C. Sun, J. S. H. Lee and M. Zhang, Magnetic nanoparticles in MR imaging and drug delivery, *Adv. Drug Delivery Rev.*, 2008, **60**(11), 1252–1265. Inorganic Nanoparticles in Drug Delivery.

5 V. I. Shubayev, T. R. Pisanic and S. Jin, Magnetic nanoparticles for theragnostics, *Adv. Drug Delivery Rev.*, 2009, **61**(6), 467–477. Identifying and Assessing Biomaterial Nanotoxicity in Translational Research for Preclinical Drug Development.

6 T. Sasaki, N. Iwasaki, K. Kohno, M. Kishimoto, T. Majima and S. I. Nishimura, *et al.*, Magnetic nanoparticles for improving cell invasion in tissue engineering, *J. Biomed. Mater. Res., Part A*, 2008, **86A**(4), 969–978.

7 J. B. Haun, T. J. Yoon, H. Lee and R. Weissleder, Magnetic nanoparticle biosensors, *Wiley Interdiscip. Rev.: Nanomed. Nanobiotechnol.*, 2010, **2**(3), 291–304.

This journal is © the Owner Societies 2024

*Phys. Chem. Chem. Phys.*, 2024, **26**, 3117–3125 | **3123**

8   T. A. P. Rocha-Santos, Sensors and biosensors based on magnetic nanoparticles, *TrAC, Trends Anal. Chem.*, 2014, **62**, 28–36.

9   Z. Zhou, L. Yang, J. Gao and X. Chen, Structure-Relaxivity Relationships of Magnetic Nanoparticles for Magnetic Resonance Imaging, *Adv. Mater.*, 2019, **31**(8), 1804567.

10  M. M. Yallapu, S. F. Othman, E. T. Curtis, B. K. Gupta, M. Jaggi and S. C. Chauhan, Multi-functional magnetic nanoparticles for magnetic resonance imaging and cancer therapy, *Biomaterials*, 2011, **32**(7), 1890–1905.

11  I. Matsui, Preparation of FePt Magnetic Nanoparticle Film by Plasma Chemical Vapor Deposition for Ultrahigh Density Data Storage Media, *Jpn. J. Appl. Phys.*, 2006, **45**(10S), 8302, DOI: **10.1143/JJAP.45.8302**.

12  X. Sun, Y. Huang and D. E. Nikles, FePt and CoPt magnetic nanoparticles film for future high density data storage media, *Int. J. Nanotechnol.*, 2004, **1**(3), 328–346.

13  T. Vimal, S. Pandey, S. K. Gupta, D. P. Singh, K. Agrahari and G. Pathak, *et al.*, Manifestation of strong magneto-electric dipolar coupling in ferromagnetic nanoparticles FLC composite: evaluation of time-dependent memory effect, *Liq. Cryst.*, 2018, **45**(5), 687–697.

14  H. Yang, W. Zou, K. (Ken) Ostrikov, C. Zhang and A. Du, Tuning electrocatalytic nitrogen reduction on supported nickel cluster via substrate phase engineering, *Appl. Surf. Sci.*, 2023, **640**, 158277 Available from: **https://www.sciencedirect.com/science/article/pii/S0169433223019578**.

15  H. Wang, L. Meng, S. Shang, H. Liu, M. Zhang and H. Wu, Nickel-constructing interfaces of multiheterostructure on self-supporting electrode for efficient overall urea-water splitting, *Appl. Surf. Sci.*, 2023, **640**, 158288 Available from: **https://www.sciencedirect.com/science/article/pii/S0169433223019682**.

16  Y. Kim, E. B. Choi and J. H. Lee, Surface modification of Ag-coated Cu particles using dicarboxylic acids to enhance the electrical conductivity of sintered films by suppressing dewetting in Ag shells, *Appl. Surf. Sci.*, 2023, **640**, 158326 Available from: **https://www.sciencedirect.com/science/article/pii/S0169433223020068**.

17  R. H. Aguilera-del Toro, F. Aguilera-Granja, A. Vega and L. C. Balbás, Structure, fragmentation patterns, and magnetic properties of small cobalt oxide clusters, *Phys. Chem. Chem. Phys.*, 2014, **16**, 21732–21741, DOI: **10.1039/C4CP03370A**.

18  R. H. Aguilera-del Toro, F. Aguilera-Granja, M. B. Torres and A. Vega, Relation between structural patterns and magnetism in small iron oxide clusters: reentrance of the magnetic moment at high oxidation ratios, *Phys. Chem. Chem. Phys.*, 2021, **23**(246), 272, DOI: **10.1039/D0CP03795H**.

19  M. B. Knickelbein, Nickel clusters: The influence of adsorbates on magnetic moments, *J. Chem. Phys.*, 2002, **116**(22), 9703–9711, DOI: **10.1063/1.1477175**.

20  M. B. Knickelbein, Nickel clusters: The influence of adsorbed CO on magnetic moments, *J. Chem. Phys.*, 2001, **115**(5), 1983–1986, DOI: **10.1063/1.1388542**.

21  B. Abdel-Ghani, B. Mouhssin and D. Meryem, Electronic and Magnetic Properties of Small Nickel Clusters and Their Interaction with CO Molecule, *J. Supercond. Novel Magn.*, 2021, **34**, 561–570.

22  C. D. Zeinalipour-Yazdi, D. J. Willock, A. Machado, K. Wilson and A. F. Lee, Impact of co-adsorbed oxygen on crotonaldehyde adsorption over gold nanoclusters: a computational study, *Phys. Chem. Chem. Phys.*, 2014, **16**, 11202–11210.

23  C. D. Zeinalipour-Yazdi, D. J. Willock, L. Thomas, K. Wilson and A. F. Lee, CO adsorption over Pd nanoparticles: A general framework for IR simulations on nanoparticles, *Surf. Sci.*, 2016, **646**, 210–220 Available from: **https://www.sciencedirect.com/science/article/pii/S003960281500206X**.

24  R. H. Aguilera-del Toro, F. Aguilera-Granja, L. C. Balbás and A. Vega, Structure, fragmentation patterns, and magnetic properties of small nickel oxide clusters, *Phys. Chem. Chem. Phys.*, 2017, **19**, 3366–3383, DOI: **10.1039/C6CP06225C**.

25  J. Vernieres, N. Tarrat, S. Lethbridge, E. Watchorn-Rokutan, T. Slater and D. Loffreda, *et al.*, Influence of air exposure on structural isomers of silver nanoparticles, *Commun. Chem.*, 2023, **6**(19), 1–5.

26  S. S. Laletina, M. Mamatkulov, A. M. Shor, E. A. Shor, V. V. Kaichev and I. V. Yudanov, Size and structure effects on platinum nanocatalysts: theoretical insights from methanol dehydrogenation, *Nanoscale*, 2022, **14**, 4145–4155.

27  B. Wang, M. Liu, Y. Wang and X. Chen, Structures and Energetics of Silver and Gold Nanoparticles, *J. Phys. Chem. C*, 2011, **115**(23), 11374–11381, DOI: **10.1021/jp201023x**.

28  S. R. Plant, L. Cao and R. E. Palmer, Atomic Structure Control of Size-Selected Gold Nanoclusters during Formation, *J. Am. Chem. Soc.*, 2014, **136**(21), 7559–7562, DOI: **10.1021/ja502769v** PMID: 24803386. .

29  D. Loffreda, D. M. Foster, R. E. Palmer and N. Tarrat, Importance of Defective and Nonsymmetric Structures in Silver Nanoparticles, *J. Phys. Chem. Lett.*, 2021, **12**(15), 3705–3711.

30  M. Gao, D. Wen, G. Cao, Y. Zhang, Y. Deng and J. Hu, Study the growth mechanism of AgNi nanoparticles by surface diffusion, *Appl. Surf. Sci.*, 2023, **640**, 158286 Available from: **https://www.sciencedirect.com/science/article/pii/S0169433223019669**.

31  A. Pajor-Świerzy, R. Socha, R. Pawłowski, P. Warszyński and K. Szczepanowicz, Application of metallic inks based on nickel-silver core-shell nanoparticles for fabrication of conductive films, *Nanotechnology*, 2019, **30**(22), 225301, DOI: **10.1088/1361-6528/ab0467**.

32  A. Pajor-Świerzy, D. Staśko, R. Pawłowski, G. Mordarski, A. Kamyshny and K. Szczepanowicz, Polydispersity *vs.* Monodispersity. How the Properties of Ni–Ag Core–Shell Nanoparticles Affect the Conductivity of Ink Coatings, *Materials*, 2021, **14**(9), 2304, Available from: **https://www.mdpi.com/1996-1944/14/9/2304**.

33  F. Peng, K. Chen, A. Yildirim, X. Xia, B. D. Vogt and M. M. Cakmak, Tunable Piezoresistivity from Magnetically Aligned Ni(Core)@Ag(Shell) Particles in an Elastomer

Matrix, *ACS Appl. Mater. Interfaces*, 2019, **11**(22), 20360–20369, DOI: **10.1021/acsami.9b04287**.

34 S. Wang, S. Niu, H. Li, K. K. Lam, Z. Wang and P. Du, *et al.*, Synthesis and controlled morphology of Ni@Ag core shell nanowires with excellent catalytic efficiency and recyclability, *Nanotechnology*, 2019, **30**(38), 385603, DOI: **10.1088/1361-6528/ab27ce**.

35 R. H. A. del Toro, P. G. Alvarado-Leyva and A. Vega, Uncovering the magnetic properties of the Ag*x*Ni*y* (*x* + *y* = 55) nanoalloys in the whole composition range, *J. Magn. Magn. Mater.*, 2019, **474**(551), 562Available from: **https://www.sciencedirect.com/science/article/pii/S0304885318324922**.

36 J. S. Kim, E. Kuk, K. N. Yu, J. H. Kim, S. J. Park and H. J. Lee, *et al.*, Antimicrobial effects of silver nanoparticles, *Nanomedicine*, 2007, **3**(1), 95–101Available from: **https://www.sciencedirect.com/science/article/pii/S1549963406003467**.

37 G. Rail and M. Lafrance, Confessions of the flesh and biopedagogies: discursive constructions of obesity on Nip/Tuck, *Med. Humanit.*, 2009, **35**(2), 76–79Available from: **https://mh.bmj.com/content/35/2/76**.

38 M. A. Raza, Z. Kanwal, A. Rauf, A. N. Sabri, S. Riaz and S. Naseem, Size- and Shape-Dependent Antibacterial Studies of Silver Nanoparticles Synthesized by Wet Chemical Routes, *Nanomaterials*, 2016, **6**(4), 74.

39 J. M. Soler, E. Artacho, J. D. Gale, A. García, J. Junquera and P. Ordejón, *et al.*, The SIESTA method foriab initio/iorderiN/imaterials simulation, *J. Phys.: Condens. Matter*, 2002, **14**(11), 2745–2779, DOI: **10.1088/0953-8984/14/11/302**.

40 J. P. Perdew, K. Burke and M. Ernzerhof, Generalized Gradient Approximation Made Simple, *Phys. Rev. Lett.*, 1996, **77**, 3865–3868, DOI: **10.1103/PhysRevLett.77.3865**.

41 N. Troullier and J. L. Martins, Efficient pseudopotentials for plane-wave calculations, *Phys. Rev. B: Condens. Matter Mater. Phys.*, 1991, **43**, 1993–2006, DOI: **10.1103/PhysRevB.43.1993**.

42 L. Kleinman and D. M. Bylander, Efficacious Form for Model Pseudopotentials, *Phys. Rev. Lett.*, 1982, **48**, 1425–1428, DOI: **10.1103/PhysRevLett.48.1425**.

43 S. G. Louie, S. Froyen and M. L. Cohen, Nonlinear ionic pseudopotentials in spin-density-functional calculations, *Phys. Rev. B: Condens. Matter Mater. Phys.*, 1982, **26**, 1738–1742, DOI: **10.1103/PhysRevB.26.1738**.

44 G. Kresse and J. Furthmüller, Efficient iterative schemes for *ab initio* total-energy calculations using a plane-wave basis set, *Phys. Rev. B: Condens. Matter Mater. Phys.*, 1996, **54**, 11169–11186.

45 G. Kresse and D. Joubert, From ultrasoft pseudopotentials to the projector augmented-wave method, *Phys. Rev. B: Condens. Matter Mater. Phys.*, 1999, **59**, 1758–1775.

46 P. Geerlings, F. De Proft and W. Langenaeker, Conceptual Density Functional Theory, *Chem. Rev.*, 2003, **103**(5), 1793–1874. PMID: 12744694.

47 R. G. Pearson, Absolute electronegativity and hardness: application to inorganic chemistry, *Inorg. Chem.*, 1988, **27**(4), 734–740.

48 P. K. Chattaraj and S. Duley, Electron Affinity, Electronegativity, and Electrophilicity of Atoms and Ions, *J. Chem. Eng. Data*, 2010, **55**(5), 1882–1886.

49 K. Ohshimo, S. Azuma, T. Komukai, R. Moriyama and F. Misaizu, Structures and CO-Adsorption Reactivities of Nickel Oxide Cluster Cations Studied by Ion Mobility Mass Spectrometry, *J. Phys. Chem. C*, 2015, **119**(20), 11014–11021.

50 G. Vinuesa, R. H. A. del Toro and A. Vega, Structural properties, magnetism and reactivity of Ni$_{13-x}$Fe$_x$ nanoalloys, *J. Magn. Magn. Mater.*, 2021, **524**, 167636 Available from: **https://www.sciencedirect.com/science/article/pii/S0304885320326032**.

51 P. Álvarez Zapatero, A. Lebon, R. H. Aguilera del Toro, A. Aguado and A. Vega, Why are Zn-rich Zn–Mg nanoalloys optimal protective coatings against corrosion? A first-principles study of the initial stages of the oxidation process, *Phys. Chem. Chem. Phys.*, 2021, **23**, 24685–24698, DOI: **10.1039/D1CP03447B**.

This journal is © the Owner Societies 2024

*Phys. Chem. Chem. Phys.*, 2024, **26**, 3117–3125 | **3125**